RESEARCH ARTICLE

Regulation of non-Hermitian couplings in a spontaneous six-wave mixing process

Zhou Feng[1], Rui Zhuang[1], Haitian Tang[1], Sinong Liu[1], Qingyu Chen[1], Feng Li[1], Kangkang Li[2,*], Yanpeng Zhang[1,*]

[1]Key Laboratory for Physical Electronics and Devices of the Ministry of Education & Shaanxi Key Lab of Information Photonic Technique, Xi'an Jiaotong University, Xi'an 710049, China

[2]State Key Laboratory for Artificial Microstructure and Mesoscopic Physics and Frontiers Science Center for Nano-optoelectronics, School of Physics, Peking University, Beijing100871, China

Corresponding authors. E-mail: *kangkangli@pku.edu.cn, *ypzhang@mail.xjtu.edu.cn

Received December 27, 2025; accepted April 15, 2026

Supporting Information

1. Triphoton State Generation via the SSWM Process

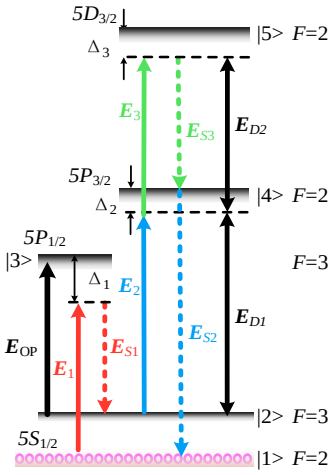

Figure S1. Energy level diagram of the SSWM process in a 5-level system of ^{85}Rb atomic vapor.

In our scheme, time–energy entangled triphotons (E_{S1}, E_{S2} and E_{S3}) are generated via a spontaneous six-wave mixing (SSWM) process, as schematically illustrated in Figure S1, implemented in a typical five-level ^{85}Rb atomic configuration. The relevant atomic states involved are $|1\rangle$ ($5S_{1/2}$ F=2), $|2\rangle$ ($5S_{1/2}$ F=3), $|3\rangle$ ($5P_{1/2}$ F=2), $|4\rangle$ ($5P_{3/2}$ F=3), and $|5\rangle$ ($5D_{3/2}$ F=2). E_1 drives the transition $|1\rangle \longrightarrow |3\rangle$ with a large red detuning. Meanwhile, two coupling fields E_2 and E_3 couple the transitions $|2\rangle \longrightarrow |4\rangle$ and $|4\rangle \longrightarrow |5\rangle$, respectively, establishing the multi-photon coherence required for the SSWM interaction. Through the Doppler-broadened SSWM process in the hot atomic vapor, backward-propagating triplet photons E_{Sj} (ω_{Sj}, κ_{Sj} with j = 1, 2, 3) are spontaneously emitted. This nonlinear process simultaneously satisfies the energy conservation condition $\omega_1 + \omega_2 + \omega_3 = \omega_{S1} + \omega_{S2} + \omega_{S3}$, and the phase-matching condition $k_1 + k_2 + k_3 = k_{S1} + k_{S2} + k_{S3}$. As a result, the generated triphotons exhibit intrinsic time–energy entanglement. In particular, when the energy of one photon (e.g., E_{S1}) is measured, the remaining two photons E_{S2} and E_{S3} are projected onto a joint state that still satisfies the same total energy constraint. Therefore, E_{S2} and E_{S3} remain entangled in the energy–time degree of freedom, even after conditioning on the detection of E_{S1}. The indistinguishability among the multiple energy gives rise to a W-state structure in the triphoton Hilbert space.

Furthermore, two external control fields, E_{D1} and E_{D2}, are introduced to coherently couple the transitions $|2\rangle \longrightarrow |4\rangle$ and $|4\rangle \longrightarrow |5\rangle$, respectively. These control beams enable flexible manipulation of the effective coupling configuration and the associated non-Hermitian energy-level structure during the SSWM process.

In the EIT-based spontaneous six-wave mixing (SSWM) process, the physics of the triphoton generation process can be explained by the nonlinear susceptibility $\chi^{(5)}$. In the interaction picture, the effective Hamiltonian of SSWM with a non-Hermitian system can be written as $H_{\text{eff}} = H_{\text{eff}-\text{F}} + H_{\text{eff}-\text{nH}}$; here $H_{\text{eff}-\text{F}}$ represents the effective Hamiltonian of SSWM in five-energy levels can be written as:

$$H_{eff-F} = -\hbar \begin{bmatrix} 0 & 0 & -\Omega_1^* & -\Omega_{S2}^* & 0 \\ 0 & \Delta_1 - \Delta_{S1} & -\Omega_{S1}^* & -\Omega_2^* & 0 \\ \Omega_1 & \Omega_{S1} & \Delta_1 & 0 & 0 \\ \Omega_{S2} & \Omega_2 & 0 & \Delta_1 - \Delta_{S1} + \Delta_2 & -\Omega_3^* - \Omega_{S3}^* \\ 0 & 0 & 0 & \Omega_3 + \Omega_{S3} & \Delta_1 - \Delta_{S1} + \Delta_2 + \Delta_3 \end{bmatrix} \tag{S1}$$

H_{effPT} represents the EIT-based non-Hermitian structure based on two coupled energy levels system $|2\rangle \rightarrow |4\rangle$ can be written as:

$$H_{eff-nH} = -\hbar \begin{bmatrix} -i\Gamma_{21} & \Omega_{D1}^* \\ \Omega_{D1} & \Delta_{D1} - i\Gamma_{41} \end{bmatrix} \tag{S2}$$

where $\Gamma_{ij} = (\Gamma_i + \Gamma_j)/2$ is the decoherence rate between $|i\rangle$ and $|j\rangle$. Γ_i represents the decay rate of the $|i\rangle$. Ω_i is the Rabi frequency induced by the optical field E_i, while Δ_i is corresponding to the associated detuning.

1.1 Fifth-Order Doppler-Broadened Nonlinear Susceptibility $\chi^{(5)}$

According to the motion equation, the density–matrix equations can be obtained to be

$$\frac{\partial}{\partial t}\rho = -\frac{i}{\hbar}[H_{\text{eff}-\text{F}}, \rho] - \Gamma\rho \tag{S3}$$

where $H_{\text{eff}-\text{F}}$ denotes the effective Hamiltonian of the five-level atomic system participating in the SSWM process, and Γ represents the phenomenological relaxation matrix incorporating spontaneous decay and dephasing processes.

For an arbitrary density-matrix element ρ_{ij}, the equation of motion follows directly from Eq. (S3):

$$\frac{\partial}{\partial t}\rho_{ij} = -\frac{i}{\hbar}\sum_k \left(H_{ik}\rho_{kj} - \rho_{ik}H_{kj}\right) - \Gamma_{ij}\rho_{ij} \tag{S4}$$

This general expression forms the basis for deriving all relevant atomic coherences contributing to the nonlinear polarization.

In the experiment, the three signal fields E_{S1}, E_{S2} and E_{S3} are generated spontaneously and are therefore much

weaker than the applied pump and control fields. We thus adopt a perturbative expansion of the density matrix in powers of the signal-field Rabi frequencies:

$$\rho = \rho^{(0)} + \rho^{(1)} + \rho^{(2)} + \cdots. \tag{S5}$$

The atomic ensemble is initially prepared in the ground state $|1\rangle$ by optical pumping, leading to the zeroth-order solution

$$\rho_{11}^{(0)} \cong 1, \rho_{ii}^{(0)} \cong 0 \quad (i \neq 1) \tag{S6}$$

with all coherences vanishing at zeroth order.

We first consider the coherence ρ_{31}, which is driven by the pump field E_1. From Eq. (S2), we obtain

$$\frac{\partial}{\partial t}\rho_{31} = -i\Omega_1\rho_{11} - (\gamma_{31} + i\Delta_1)\rho_{31} \tag{S7}$$

where γ_{31} is the decoherence rate and Δ_1 is the detuning of E_1.

Under steady-state conditions ($\frac{\partial}{\partial t}\rho_{31} = 0$), the first-order solution reads

$$\rho_{31}^{(1)} = \frac{-i\Omega_1}{\gamma_{31}+i\Delta_1} \tag{S8}$$

The signal field E_{S1} couples the coherence ρ_{31} to ρ_{21}. The equation of motion for ρ_{21} is

$$\frac{\partial}{\partial t}\rho_{21} = -i(\Omega_{S1}^*\rho_{31} + \Omega_2^*\rho_{41}) - [\gamma_{21} + i(\Delta_1 - \Delta_{S1})]\rho_{21} \tag{S9}$$

Retaining only the lowest-order contribution and substituting Eq. (S8), we obtain

$$\rho_{21}^{(2)} = \frac{-\Omega_1\Omega_{S1}^*}{(\gamma_{31}+i\Delta_1)[\gamma_{21}+i(\Delta_1-\Delta_{S1})]} \tag{S10}$$

This coherence represents a Raman-type ground-state coherence induced by the joint action of E_1 and E_{S1}.

The coupling field E_2 transfers the coherence ρ_{21} to the excited state $|4\rangle$. The corresponding equation reads

$$\frac{\partial}{\partial t}\rho_{41} = -i(\Omega_2\rho_{21} + \Omega_{S2}\rho_{11}) - [\gamma_{41} + i(\Delta_1 - \Delta_{S1} + \Delta_2)]\rho_{41} \tag{S11}$$

Under steady-state conditions, the third-order solution is

$$\rho_{41}^{(3)} = \frac{-i\Omega_2\rho_{21}^{(2)}}{\gamma_{41}+i(\Delta_1-\Delta_{S1}+\Delta_2)} \tag{S12}$$

The field E_3 further couples $|4\rangle$ to $|5\rangle$, yielding

$$\frac{\partial}{\partial t}\rho_{51} = -i\Omega_3\rho_{41} - [\gamma_{51} + i(\Delta_1 - \Delta_{S1} + \Delta_2 + \Delta_3)]\rho_{51} \tag{S13}$$

The steady-state fourth-order coherence is therefore

$$\rho_{51}^{(4)} = \frac{-i\Omega_3\rho_{41}^{(3)}}{\gamma_{51}+i(\Delta_1-\Delta_{S1}+\Delta_2+\Delta_3)} \tag{S14}$$

Finally, the emission of the third signal photon E_{S3} is associated with the coherence ρ_{54}, whose equation of motion is

$$\frac{\partial}{\partial t}\rho_{54} = -i\Omega_{S3}\rho_{41} - [\gamma_{54} + i(\Delta_1 - \Delta_{S1} + \Delta_2 + \Delta_3 - \Delta_{S3})]\rho_{54} \tag{S15}$$

Solving in the steady-state limit and substituting the lower-order coherences, we obtain

$$\rho_{54}^{(5)} = \frac{i\Omega_3\rho_{41}^{(3)}}{\begin{matrix}(\gamma_{31}+i\Delta_1)[\gamma_{21}+i(\Delta_1-\Delta_{S1})][\gamma_{41}+i(\Delta_1-\Delta_{S1}+\Delta_2)] \\ [\gamma_{51}+i(\Delta_1-\Delta_{S1}+\Delta_2+\Delta_3)][\gamma_{54}+i(\Delta_1-\Delta_{S1}+\Delta_2+\Delta_3-\Delta_{S3})]\end{matrix}} \tag{S16}$$

where the product runs over all intermediate virtual states involved in the SSWM process.

Consequently, the fifth-order Doppler-broadened nonlinear susceptibility $\chi^{(5)}$ in the SSWM process can be identified as:

$$\chi^{(5)}(\delta_2, \delta_3) = \int dv \frac{2f(v)Ni\mu_{13}\mu_{23}\mu_{24}\mu_{45}^2\mu_{14}}{\varepsilon_0\hbar^5\left[\begin{matrix}(\Gamma_{31}+i\Delta_{B1})(\Gamma_{21}+iW_{D-}\delta_2+iW_{D+}\delta_3)(\Gamma_{41}+i\Delta_{B2}+iW_{D-}\delta_2+iW_{D+}\delta_3) \\ (\Gamma_{51}+i\Delta_{B2}+i\Delta_{B3}+iW_{D-}\delta_2+iW_{D+}\delta_3)(\Gamma_{41}+i\Delta_{B2}+iW_{D-}\delta_2+d_1+d_2)\end{matrix}\right]} \tag{S17}$$

Here $f(v) = \sqrt{\frac{m_{Rb}}{2\pi k_B T}} \exp\left[-\frac{m_{Rb}v^2}{2k_B T}\right]$ is the Maxwell-Boltzmann velocity distribution of the Rb atoms in the thermal motion, where m_{Rb} is the mass of the Rb atom, k_B is the Boltzmann constant, T is the vapor temperature, and v is the atomic kinetic velocity; N is atomic density, μ_{ij} (i, j=1,2,3,4,5) refers to the electric dipole matrix elements for the atomic transition $|i\rangle \rightarrow |j\rangle$, $\Gamma_{\mathrm{ij}} = \left(\Gamma_{\mathrm{i}} + \Gamma_{\mathrm{j}}\right)/2$ is the decoherence rate between levels $|i\rangle$ and $|j\rangle$; $\Delta_{Bi} = \Delta_i + v\omega_{ij}/c$ with frequency detuning $\Delta_i = \omega_{ij} - \omega_i$, and ω_{ij} being the frequency between levels $|i\rangle$ and $|j\rangle$; $W_{D\pm} = 1 \pm v/c$ accounts for the first-order Doppler shift which depends on atomic velocity with c the speed of light in vacuum, c is the speed of light in the vacuum; Ω_{D1} and Ω_{D2} are the Rabi frequency of E_{D1} and E_{D2}; δ_i represents the deviations around the corresponding central frequency ϖ_{Si} of generated photons that is $\omega_{Si} = \varpi_{Si} + \delta_i$ (i=1, 2) where $|\delta_i| \ll \varpi_{Si}$. Furthermore, it is essential to recognize that, due to the energy conservation in SSWM, the generation of these two photons is contingent upon the detection of the output E_{S1} photon at the frequency $\omega_{S1} = \omega_1 + \omega_2 + \omega_3 - \omega_{S2} - \omega_{S3}$. This necessitates that the spectral distributions of the entangled triphoton state must satisfy the condition $\delta_1 + \delta_2 + \delta_i = 0$ [1].

To enhance the fifth-order nonlinear interaction, a length of L=7 cm ^{85}Rb vapor cell is heated to 80°C using a resistive heating tape [2]. At this temperature, the Doppler broadening is estimated to be approximately Δ_D= 555 MHz, which is several orders of magnitude larger than the Rb natural linewidth [2]. The atomic density is calculated to be N=1.2×10^{11} cm^{-3}, based on $N = P/(k_B T)$, where P is the saturated vapor pressure and k_B is the Boltzmann constant. The optical depth (OD), defined as $OD = N\sigma_{41}L$, has a value of 4.6, where $\sigma_{41} = 3\pi N\Gamma_{41}c^2/(2\Delta_D\omega_{41}^2)$ is the on-resonance absorption cross-section for the transition $|1\rangle \longrightarrow |4\rangle$ [3]. When the temperature is increased to 115°C, the OD rises to 45.7.

By analyzing the fifth-order Doppler-broadened nonlinear susceptibility $\chi^{(5)}$ under various coupling configurations, we identify a distinct evolution in the system's optical response as the Rabi frequencies of the control fields are increased. This evolution signifies a transition from the weak coupling regime, where light-matter interaction is dominated by dissipative dynamics, to the strong coupling regime, characterized by coherent splitting of energy levels. Correspondingly, the temporal profile of the triphoton correlation function transforms—from an anti-bunching distribution to damped Rabi oscillations, which arise from quantum interference among multiple resonant generation pathways. Figure S2(a) shows $\chi^{(5)}$ as a function of the eigenvalues δ_2 and δ_3 in the weak coupling regime. In this case, $\chi^{(5)}$ displays a single dominant resonance peak, consistent with the presence of a single effective photon-generation pathway. As the Rabi frequency of the E_{D1} field increases and the coupling between states $|2\rangle$ and $|4\rangle$ enters the strong coupling regime, the nonlinear response evolves: $\chi^{(5)}$ develops two distinct resonant features along δ_2 direction, as shown in Figure S2(b). Similarly, $\chi^{(5)}$ develops two distinct resonant features along δ_3 direction with the increasing Rabi frequency of the E_{D2} field, which is shown in Figure S2(c).

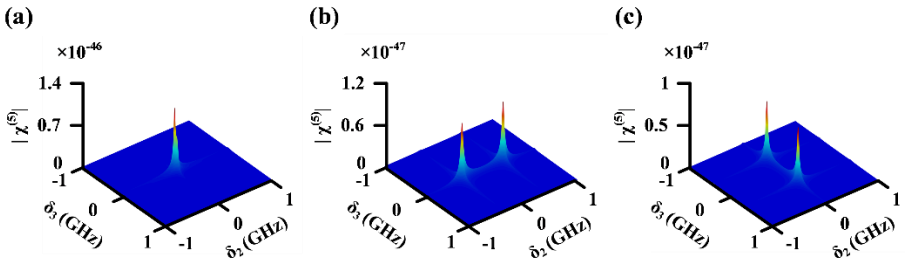

Figure S2. Simulated fifth-order nonlinear susceptibility $\chi^{(5)}$ under various coupling conditions, illustrating the transition from weak to strong coupling regimes. (a) $\chi^{(5)}$ in regime A of Figure 1(e) in the main text, corresponding to the weak coupling case with a single dominant resonance. (b) and (c), and (d) show $\chi^{(5)}$ in regimes B, C, in the Figure 1(e) of main part, respectively. Simulation parameters are set as follows: $\Gamma_{54} = 2\pi \times 0.66$ MHz, $\Gamma_{31} = \Gamma_{41} = 2\pi \times 6$ MHz, $\Gamma_{11} = \Gamma_{22} = 0.4 \times \Gamma_{41}$, and $\Gamma_{21} = 0.2 \times \Gamma_{41}$.

1.2 Doppler-Broadened Linear Susceptibility

According to Figure S1, the respective linear susceptibilities for E_{S1}, E_{S2} and E_{S3} have been determined as: [4]

$$\chi_{S1} = \int f(v) \frac{iN\mu_{32}^2}{\varepsilon_0\hbar\left[\Gamma_{32}+\left(1-\frac{v}{c}\right)i\delta_1+i\Delta_1+\frac{|\Omega_2|^2}{\Gamma_{42}+\left(1-\frac{v}{c}\right)i\delta_1+i\Delta_1+i\Delta_2+\frac{|\Omega_3|^2}{\Gamma_{54}+\left(1-\frac{v}{c}\right)i\delta_1+i\Delta_1+i\Delta_2+i\Delta_3}}\right]}dv \tag{S18}$$

$$\chi_{S2} = \int f(v) \frac{iN\mu_{14}^2}{\varepsilon_0\hbar\left[\Gamma_{41}+\left(1-\frac{v}{c}\right)i\delta_2+i\Delta_2+\frac{|\Omega_2|^2}{\Gamma_{44}+\left(1-\frac{v}{c}\right)i\delta_2}+\frac{|\Omega_3|^2}{\Gamma_{54}+\left(1-\frac{v}{c}\right)i\delta_2+i\Delta_2+i\Delta_3}\right]}dv, \tag{S19}$$

$$\chi_{S3} = \int f(v) \frac{iN\mu_{54}^2}{\varepsilon_0\hbar\left[\Gamma_{54}+\left(1-\frac{v}{c}\right)i\delta_3+i\Delta_3+\frac{|\Omega_3|^2}{\Gamma_{44}+\left(1-\frac{v}{c}\right)i\delta_3}+\frac{|\Omega_2|^2}{\Gamma_{41}+\left(1-\frac{v}{c}\right)i\delta_3+i\Delta_3+i\Delta_2}\right]}dv. \tag{S20}$$

Based on the relationship ($V_g = c/(n(\omega) + \delta d(\mathrm{Re}[\chi_{si}(\delta)])/d\delta)$) between group velocity and linear susceptibilities [1,5], we can get the group velocity of E_{S2} and E_{S3}:

$$v_{g(S1)} = \frac{2k_{32}Lc}{\omega_{32}OD\Gamma_{32}} \frac{\left[{A_1}^2+(\Gamma_{32}\Gamma_{54})^2\right]^2}{\left[(\Gamma_{32}+\Gamma_{42})A_1-\Gamma_{32}\Gamma_{42}B_1\right]\left[{A_1}^2+(\Gamma_{32}\Gamma_{54})^2\right]} \tag{S21}$$

$$v_{g(S2)} = \frac{2k_{41}Lc}{\omega_{41}OD\Gamma_{41}} \frac{\left[A_2^2+(\Gamma_{54}\Gamma_{41})^2\right]^2}{\left[(\Gamma_{54}+\Gamma_{44})A_2-\Gamma_{44}\Gamma_{54}B_2\right]\left[A_2^2+(\Gamma_{54}\Gamma_{41})^2\right]} \tag{S22}$$

$$v_{g(S3)} = \frac{2k_{54}Lc}{\omega_{54}OD\Gamma_{54}} \frac{\left[A_3^2+(\Gamma_{41}\Gamma_{54})^2\right]^2}{\left[(\Gamma_{54}+\Gamma_{44})A_3-\Gamma_{44}\Gamma_{54}B_3\right]\left[A_3^2+(\Gamma_{41}\Gamma_{54})^2\right]} \tag{S23}$$

Where $A_1 = \Gamma_{54}\Gamma_{32}\Gamma_{42} + |\Omega_2|^2\Gamma_{54} + |\Omega_3|^2\Gamma_{42}$, $B_1 = \Gamma_{54}(\Gamma_{32} + \Gamma_{42}) + \Gamma_{32}\Gamma_{42} + |\Omega_2|^2 + |\Omega_3|^2$,

$A_2 = \Gamma_{54}\Gamma_{41}\Gamma_{44} + |\Omega_2|^2\Gamma_{54} + |\Omega_3|^2\Gamma_{44}$, $B_2 = \Gamma_{54}(\Gamma_{41} + \Gamma_{44}) + \Gamma_{41}\Gamma_{44} + |\Omega_2|^2 + |\Omega_3|^2$, $A_3 = \Gamma_{41}\Gamma_{54}\Gamma_{44} + |\Omega_3|^2\Gamma_{41} + |\Omega_2|^2\Gamma_{44}$, and $B_3 = \Gamma_{41}(\Gamma_{54} + \Gamma_{44}) + \Gamma_{54}\Gamma_{44} + |\Omega_3|^2 + |\Omega_2|^2$.

2. Non-Hermitian System

Based on the non-Hermitian laser–atom coupling configuration described in the Eq. (S2), we derive its eigenvalue equation. The eigenvalues δ of the Hamiltonian satisfy the characteristic equation:

$$H_{eff-nH}\psi = \delta\psi \tag{S24}$$

This leads to the secular equation $\det(H_{eff-nH} - \delta I) = 0$, where I is the identity matrix.

For convenience, we introduce the average decoherence rate ($\Gamma_{effa} = (\Gamma_{21} + \Gamma_{41})/2$) and differential decoherence rate ($\Gamma_{\mathrm{di}ffa} = (\Gamma_{21} - \Gamma_{41})/2$). To simplify the quadratic equation, we shift the eigenvalue variable as:

$$\delta = \frac{\Delta_{D1}}{2} - i\Gamma_{effa} + x \tag{S25}$$

where x satisfies $x^2 = \Omega_{D1}^2 + \left(\Delta_{D1}/2 - i\Gamma_{diffa}\right)^2$. Therefore, the eigenvalues of the non-Hermitian Hamiltonian are:

$$\delta_{D1\pm} = \Delta_{D1}/2 - i\Gamma_{effa} \pm \sqrt{\Omega_{D1}^2 + \left(\Delta_{D1}/2 - i\Gamma_{diffa}\right)^2} \tag{S26}$$

Using the energy-level structure shown in Figure S1 and the eigenvalues of the non-Hermitian Hamiltonian, we numerically evaluate the variation of the eigenvalue under different modulation parameters.

Figure S3 illustrates the evolution of the eigenvalues of the system as functions of both the Rabi frequency (Ω) and detuning (Δ) of the control optical field, focusing on the real part ($\mathrm{Re}(\delta)$) and imaginary part ($\mathrm{Im}(\delta)$) of the eigenvalues. As Ω increases, the real components of the eigenvalues transition from a single branch to two separated branches, signaling the emergence of dressed-state splitting and entry into the strong coupling regime. Simultaneously, the imaginary components—initially distinct—merge into a single degenerate value, indicating the presence of an exceptional point (EP) where the decay rates of the eigenstates coalesce. The detuning Δ also plays a critical role in

shaping the non-Hermitian eigenvalue. When $\Delta = 0$, the eigenvalue δ_{D1} associated with the dressed state E_{S2} exhibits characteristic signatures that depend on the coupling strength: either a single-valued or split real component and either coalesced or distinct imaginary components. When $\Delta \neq 0$, both the real and imaginary parts of δ_{D1} evolve continuously with detuning, reflecting the interplay between coherent coupling and dissipative dynamics in the non-Hermitian regime.

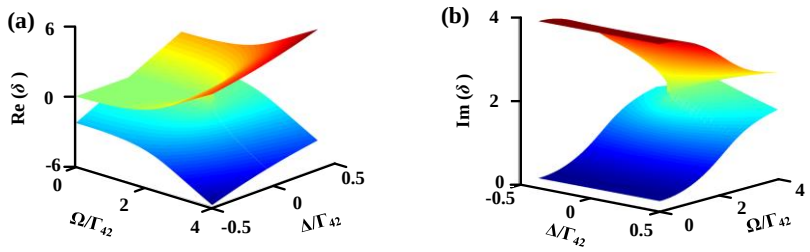

Figure S3. (a) and (b) represent the real and imaginary parts of the eigenenergy nature of E_{S2} under non-Hermitian interaction, respectively. $\Gamma_{21} = 0.2 \cdot \Gamma_{41}$.

The optical field E_{D2} regulates the coupling dynamics between atomic energy levels $|4\rangle$ and $|5\rangle$. The effective non-Hermitian structure Hamiltonian describing this subsystem can be written as [6,7]:

$$H_{nH-D2} = \begin{bmatrix} \Delta_2 - i\Gamma_{41} & \Omega_{D2} \\ \Omega_{D2} & \Delta_2 - \Delta_{D2} - i\Gamma_{51} \end{bmatrix} \tag{S27}$$

Ω_{D2} is the Rabi frequency induced by the optical field E_{D2}, while Δ_{D2} is the corresponding associated detuning. Similar to solving the eigenvalue equation of H_{eff-nH}, the eigenvalues of H_{nH-D2} are $\delta_{D2\pm} = \Delta_b/2 - i\Gamma_{effb} \pm \sqrt{\Omega_{D2}^2 + \left(\Delta_b/2 - i\Gamma_{diffb}\right)^2}$. $\Gamma_{effb} = (\Gamma_{41} + \Gamma_{51})/2$, $\Gamma_{diffb} = (\Gamma_{41} - \Gamma_{51})/2$ and $\Delta_b = 2\Delta_2 - \Delta_{D2}$. Similarly, the complex eigenvalues of H_{nH-D2} also have different resonant components when $\Omega_{D2} > \Gamma_{diffb}$, indicating that the system operates in the strong coupling regime (the right part in Figures S4 (a) and (b)). The imaginary components for the two resonant eigenstates coalesce when $\Omega_{D2} = \Gamma_{diffb}$, signifying eigenstate degeneracy as shown in the middle regime of Figure S4, while it enters the weak coupling regime when $\Omega_{D2} < \Gamma_{diffb}$. This non-Hermitian framework provides crucial insight into how tuning the Rabi frequency of E_{D2} modulates the quantum correlations of the generated triphoton state through manipulation of the dressed-state structure.

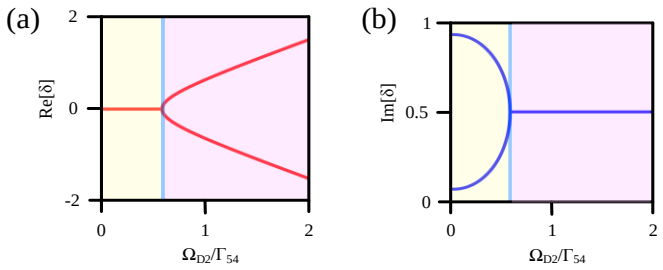

Figure S4. (a) and (b) Eigenvalue diagram for the real part and imaginary parts as functions of Ω_{D2}/Γ_{51}.

As the Rabi frequency Ω_{D1} increases, the system enters the intermediate regime (middle region in Figure 1c), where the eigenvalue spectrum exhibits one real and one imaginary component—a hallmark of the exceptional point (EP). In this regime, the bandwidth is approximately comparable to the effective parameters ($\Delta\omega_{g2} \approx [|\Omega_{e2}|, \Gamma_{eff2}]$). Upon further increase of Ω_{D1}, the system reaches the strong coupling regime (right region in Figure S4), where the eigenvalues contain two real parts and one imaginary part. The system satisfies $\Delta\omega_{g2} \gg [|\Omega_{e2}|, \Gamma_{eff2}]$. In this strong coupling regime, two real parts of the eigenvalue are $\lambda_+ = -0.5 * \left(\Delta_{D1} + \sqrt{\Delta_{D1}^2 + 4|\Omega_{D1}|^2}\right)$ and $\lambda_- = -0.5 *$

$\left(\Delta_{D1} - \sqrt{\Delta_{D1}^2 + 4|\Omega_{D1}|^2}\right)$. Meanwhile, the gap between these two parts is $\Delta_{G2} = \sqrt{\Delta_{D1}^2 + 4|\Omega_{D1}|^2}$. Figure S5 illustrates the dependence of these two real parts of the eigenvalue on the Rabi frequency of the regulating optical field. The red curve represents the splitting behavior at a detuning of $\Delta_D = 50$ MHz, while the black curve corresponds to $\Delta_D = 200$ MHz. As shown in the figure, the gap between two real parts increases nonlinearly with the Rabi frequency, following an approximately exponential trend. Notably, when the Rabi frequency is relatively small, the energy gap between two real parts is larger for the case with greater detuning ($\Delta_D = 200$ MHz). These results highlight the tunability of the non-Hermitian adjusting via both Rabi frequency and detuning, offering a versatile control knob for manipulating light–matter interactions in non-Hermitian quantum systems.

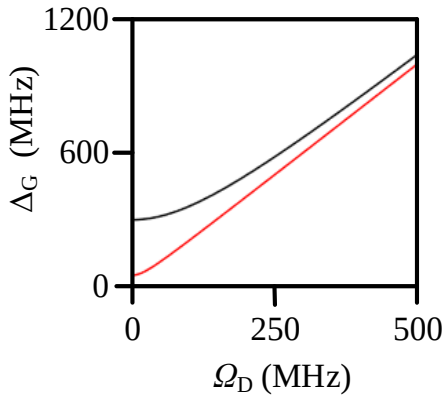

Figure S5. The distance Δ_G between two sub-levels as a function of Ω_D. The black line represents Δ_D=200 MHz, and the red line represents Δ_D=50 MHz.

3. Coincidence counting of triphotons

To compute the resultant triphoton state generated through the spontaneous six-wave mixing (SSWM) process, we analyze the triphoton coincidence counting rate under various energy level configurations at the output surfaces of the interaction medium. The interaction Hamiltonian governing the triphoton generation, within the rotating-wave approximation and neglecting surface reflections, is defined as:[2,8,9]

$$H = \varepsilon_0 \int_V d^3r \chi^{(5)} E_1 E_2 E_3 E_{S3}^{(-)} E_{S2}^{(-)} E_{S1}^{(-)} + H.c \tag{S28}$$

$\chi^{(5)}$ represents the fifth-order Doppler-broadened nonlinear susceptibility, V is the interaction volume illuminated by the input fields, and $H.c$ is the Hermitian conjugate [10]. The state vector of the triphotons can be derived using first-order perturbation theory in the Schrödinger picture and can be formulated as follows: [2]

$$|\psi\rangle = \iiint d\omega_{S1} d\omega_{S2} d\omega_{S3} \chi^{(5)} \Phi\left(\frac{\Delta KL}{2}\right) \delta(\Delta\omega) |\omega_{S1}, \omega_{S2}, \omega_{S3}\rangle \tag{S29}$$

Here, $\Delta\omega = \omega_{S1} - \omega_1 + \omega_{S2} - \omega_2 + \omega_{S3} - \omega_3$; $\Phi(\Delta KL/2) = \mathrm{sinc}(\Delta kL/2) e^{-i\Delta kL/2}$ is the phase-mismatch longitudinal function which ascribes the triphoton natural spectral width arising from their different group velocities; L is the interaction length; $\Delta k = \Delta\vec{k} \cdot \hat{z}$ is the phase mismatch; Dirac function (δ) is derived from the time integral in the steady-state approximation, ensuring the energy conservation in the SSWM process [1].

3.1 Coincidence counting of triphotons

The triphoton coincidence counting is described by the equation:

$$R_3 = \left|\langle 0 | E_{S3}^{(+)}(\tau_3) E_{S2}^{(+)}(\tau_2) E_{S1}^{(+)}(\tau_1) |\Psi\rangle\right|^2 = \left|G^{(3)}(\tau_{21}, \tau_{31})\right|^2 \tag{S30}$$

where $G^{(3)}(\tau_{21}, \tau_{31}) = A \sum_{KS1} \sum_{KS2} \sum_{KS3} e^{-ip} F(k_{S1}, k_{S2}, k_{S3})$ is often referred to as the triphoton amplitude, $p = \omega_{S1}\tau_1 + \omega_{S2}\tau_2 + \omega_{S3}\tau_3$, where all slowly varying terms and constants have been absorbed into A. $F(k_{S1}, k_{S2}, k_{S3}) = \varsigma \chi^{(5)} \Phi(\Delta KL) \delta(\Delta\omega)$, $\Delta\omega = \omega_1 + \omega_2 + \omega_3 - \omega_{S1} - \omega_{S2} - \omega_{S3}$, with ς being a grouped constant, where Dirac δ

function comes from the time integral in the steady-state approximation, ensuring the energy conservation in the SSWM process. $\Phi(\Delta KL) = sin\,c\,[\Delta k(\delta_2, \delta_3)L/2]$ [11-13].

The conditional two-photon coincidence counting is described by the equation:

$$R_2 = \sum_{K_{S2}} \left| a_{K_{S2}} \langle 0 | E_{S1}^{(+)}(\tau_1) E_{S3}^{(+)}(\tau_3) | \Psi \rangle \right|^2 = \sum_{K_{S2}} \left| G^{(3)}(\tau_{31}) \right|^2 \quad \text{(S31)}$$

assuming, for instance, that the E_{S2} photons are traced away. Notably, $G^{(3)}(\tau_{31})$ also represents the triphoton amplitude, even though one subsystem is not detected in the experiment. And $G^{(3)}(\tau_{31}) = \mathrm{A}_2 \sum_{KS1} \sum_{KS3} e^{-i(\omega_{S1}\tau_1 + \omega_{S3}\tau_3)} F(k_{S1}, k_{S2}, k_{S3})$, where all the slowly varying terms and constants have been grouped into A_2. $F(k_{S1}, k_{S2}, k_{S3}) = C\chi^{(5)}\Phi(\Delta KL)\delta(\omega_1 + \omega_2 + \omega_3 - \omega_{S1} - \omega_{S2} - \omega_{S3})$, $\Phi(\Delta KL) = sin\,c\,[\Delta k(\delta_2, \delta_3)L/2]$ [11-13].

3.2 Waveform of Triphotons in SSWM

In the process of spontaneous four-wave mixing (SFWM) generation, the biphoton wave function in the interaction picture is known to arise from the convolution of nonlinear and linear optical responses [14]. Depending on which contribution dominates, the biphoton temporal correlation can be categorized into two regimes: the damped Rabi oscillation regime and the group delay regime [15].

Analogously, the triphoton wavefunction generated via spontaneous six-wave mixing (SSWM) in the interaction picture is also described by a convolution of nonlinear and linear responses along each detection dimension, corresponding to the time delays $\tau_{21} = \tau_2 - \tau_1$ and $\tau_{31} = \tau_3 - \tau_1$. These two directions represent the temporal correlations between the photon pairs (E_{S1}, E_{S2}) and (E_{S1}, E_{S2}), respectively. In a five-level atomic system used for triphoton generation, the respective emission processes of photons E_{S2} and E_{S3} are largely governed by independent coupling paths. This weak mutual influence implies that the correlation waveforms along τ_{21} and τ_{31} evolve essentially independently, allowing each direction to reveal distinct nonlinear and non-Hermitian features of the SSWM process.

When the Rabi frequency Ω_{D1} modulates the coupling between energy levels $|2\rangle$ and $|4\rangle$, the resulting triphoton temporal correlations exhibit qualitatively distinct behaviors governed by the non-Hermitian eigenvalue structure. Within the SSWM process, three coupling regimes can be identified depending on the relative magnitude of Ω_{D1} and the dissipation rate $\Gamma_{\mathrm{diff}a}$.

In the weak-coupling regime ($\Omega_{D1} < \Gamma_{\mathrm{diff}a}$, regime A in Figure 1 (e) of the main part), the imaginary parts of the two resonant eigenvalues coalesce while their real parts remain nondegenerate, indicating that the system is dominated by loss. Under this condition, the coupling between $|2\rangle$ and $|4\rangle$ is weak, and the corresponding triphoton coincidence count is described by

$$G^{(3)}(\tau_{21}, \tau_{31}) = Ce^{-2(\Gamma_{eff}\tau_{21} + \Gamma_3\tau_{31})/W_D} \sinh^2\left(\frac{\Omega_e\tau_{21}}{W_D}\right)\Theta(\tau_{21})\Theta(\tau_{31}) \quad \text{(S32)}$$

At the critical point ($\Omega_{D1} = \Gamma_{\mathrm{diff}a}$, regime AB in Figure 1 (e) of the main part), both the real and imaginary parts of the eigenvalues become degenerate, signaling the emergence of an exceptional point (EP). In this regime, the energy levels $|2\rangle$ and $|4\rangle$ undergo a non-Hermitian phase transition, and the triphoton coincidence function reduces to a single-exponential form,

$$G^{(3)}(\tau_{21}, \tau_{31}) = Bk_0^2 v_{g2}^2 e^{-2(\alpha_1 v_{g2}\tau_{21} + \Gamma_3\tau_{31})/W_D}\Theta(\tau_{21})\Theta(\tau_{31}) \quad \text{(S33)}$$

which is a hallmark of EP-induced critical dynamics.

In the strong-coupling regime ($\Omega_{D1} > \Gamma_{\mathrm{diff}a}$, regime B in Figure 1 (e) of the main part), the complex eigenvalues of the non-Hermitian Hamiltonian H_{nH-D1} split into distinct resonance branches, indicating coherent coupling between $|2\rangle$ and $|4\rangle$. The corresponding triphoton coincidence count exhibits damped oscillatory behavior,

$$G^{(3)}(\tau_{21}, \tau_{31}) = Ae^{-2(\Gamma_{eff}\tau_{21} + \Gamma_3\tau_{31})/W_D}\left[1 - cos\left(\frac{\Omega_e\tau_{21}}{W_D}\right)\right]\Theta(\tau_{21})\Theta(\tau_{31}) \quad \text{(S34)}$$

Figure S6 presents numerical simulations of the triphoton coincidence distributions under these distinct coupling conditions, highlighting the unique quantum correlation features associated with different non-Hermitian mechanisms. In Figure S6(a), the coincidence distribution calculated from Eq. (S32) exhibits pronounced antibunching along both the τ_{21} and τ_{31} axes, with the maximum coincidence probability shifted away from $\tau_{21} = \tau_{31} = 0$. This behavior is characteristic of the weakly coupled, loss-dominated regime. The corresponding two-photon coincidence projections are shown in Figures S6(a1) and (a2).

Figure S6(b) corresponds to the exceptional point, evaluated using Eq. (S33). At this singularity, the merging of the real and imaginary parts of the eigenvalues places the system at the critical boundary between weak and strong coupling. Consequently, the triphoton correlation exhibits a symmetric single-exponential decay along the τ_{21} direction, while maintaining antibunching along τ_{31}. This behavior is further corroborated by the two-photon coincidence distributions in Figures S6(b1) and (b2), where the single-mode exponential decay is observed exclusively along τ_{21}, confirming that only the $|2\rangle \leftrightarrow |4\rangle$ coupling resides at the exceptional point.

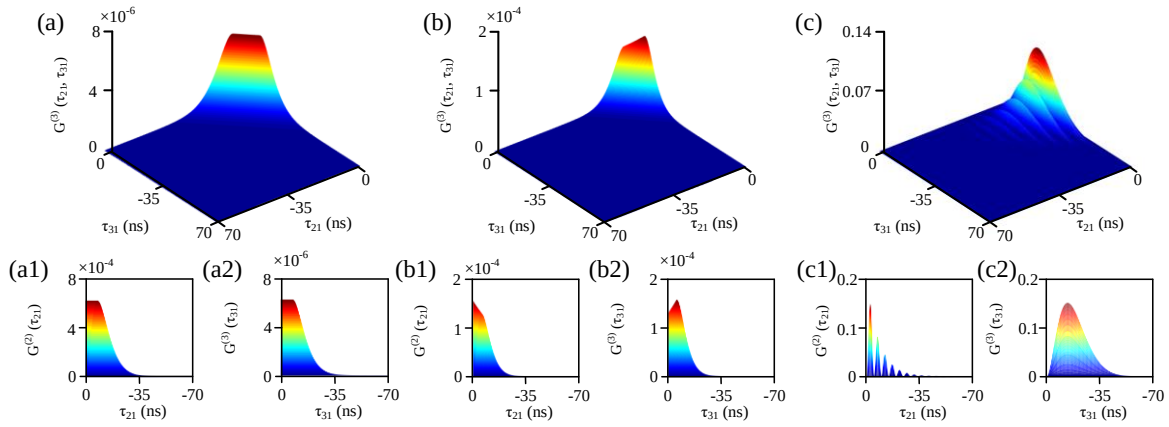

Figure S6. Simulation results of coincidence counts of time-energy-entangled W-triphoton state under various energy level coupling states. The upper panels (a–c) present the three-dimensional distribution of triphoton plotted in the (τ_{21}, τ_{31}) parameter space. The corresponding lower subfigures (a1–c1) and (a2–c2) display the conditional two-photon coincidence counts for (a-c) in τ_{21} and τ_{31} directions, respectively. (a) triphoton generated in the regime A in Figure 1(e) of the main part. (b) and (c) triphoton are generated in regimes AB and B, respectively. Simulation parameters are set as follows: $\Gamma_{54} = 2\pi \times 0.66$ MHz, $\Gamma_{31} = \Gamma_{41} = 2\pi \times 6$ MHz, $\Gamma_{11} = \Gamma_{22} = 0.4 \times \Gamma_{41}$, and $\Gamma_{21} = 0.2 \times \Gamma_{41}$.

Figure S6(c) shows the system in a strong coupling regime between $|2\rangle$ and $|4\rangle$, corresponding to regime B. Here, the triphoton correlation exhibits damped Rabi oscillations along τ_{21}, while still showing anti-bunching along τ_{31}. The conditional two-photon coincidences in Figures S6(c1) and S6(c2) confirm this behavior, indicating that the $|2\rangle \leftrightarrow |4\rangle$ transition resides in the strong coupling regime.

When the Rabi frequency Ω_{D2} modulates the coupling between energy levels $|4\rangle$ and $|5\rangle$, the RCC exhibits qualitatively different behaviors determined by the corresponding non-Hermitian eigenvalue structure. In the weak-coupling regime ($\Omega_{D2} < \Gamma_{diffb}$, regime A in Figure 1 (e) of the main part), the imaginary parts of the two resonant eigenvalues coalesce while their real parts remain distinct, indicating a loss-dominated coupling between $|4\rangle$ and $|5\rangle$. Under this condition, the triphoton coincidence count is given by

$$G^{(3)}(\tau_{21}, \tau_{31}) = Ce^{-2(\Gamma_2\tau_{21} + \Gamma_{eff}\tau_{31})/W_D} \sinh^2\left(\frac{\Omega_e \tau_{31}}{W_D}\right) \Theta(\tau_{21})\Theta(\tau_{31}) \quad \text{(S32)}$$

At the critical point ($\Omega_{D2} = \Gamma_{diffb}$, , regime AC in Figure 1 (e) of the main part), both the real and imaginary parts of the eigenvalues become degenerate, signaling the formation of an exceptional point (EP) associated with the $|4\rangle \leftrightarrow |5\rangle$ transition. In this EP regime, the triphoton coincidence function simplifies to a single-exponential form,

$$G^{(3)}(\tau_{21},\tau_{31}) = Bk_0^2 v_{g2}^2 e^{-2(\Gamma_2\tau_{21}+\alpha_2 v_{g2}\tau_{31})/W_D}\Theta(\tau_{21})\Theta(\tau_{31}) \quad \text{(S33)}$$

In the strong-coupling regime ($\Omega_{D2} > \Gamma_{diffb}$, regime C in Figure 1 (e) of the main part), the complex eigenvalues of the non-Hermitian Hamiltonian split into distinct resonance branches, indicating coherent coupling between energy levels $|4\rangle$ and $|5\rangle$. The corresponding triphoton coincidence count exhibits damped oscillatory behavior,

$$G^{(3)}(\tau_{21},\tau_{31}) = Ae^{-2(\Gamma_2\tau_{21}+\Gamma_{eff}\tau_{31})/W_D}\left[1-cos\left(\frac{\Omega_e\tau_{31}}{W_D}\right)\right]\Theta(\tau_{21})\Theta(\tau_{31}) \quad \text{(S34)}$$

Figure S7 summarizes the simulated triphoton coincidence distributions under these distinct coupling conditions. In Figure S7(a), the distribution calculated from Eq. (S32) exhibits pronounced antibunching along both the τ_{21} and τ_{31} axes, with the maximum coincidence probability significantly displaced from $\tau_{21} = \tau_{31} = 0$, consistent with a weakly coupled, loss-dominated regime. The corresponding conditional two-photon coincidence counts are shown in Figures S7(a1) and (a2). Figure S7(b) corresponds to the EP regime of the $|4\rangle \leftrightarrow |5\rangle$ transition. At this singular point, the coalescence of the real and imaginary parts of the eigenvalues leads to a single-exponential decay of the triphoton coincidence function along the τ_{31} direction, while antibunching along τ_{21} persists. This directional asymmetry is further confirmed by the conditional two-photon coincidence distributions in Figures S7(b1) and (b2), demonstrating that only the $|4\rangle \leftrightarrow |5\rangle$ coupling satisfies the EP condition.

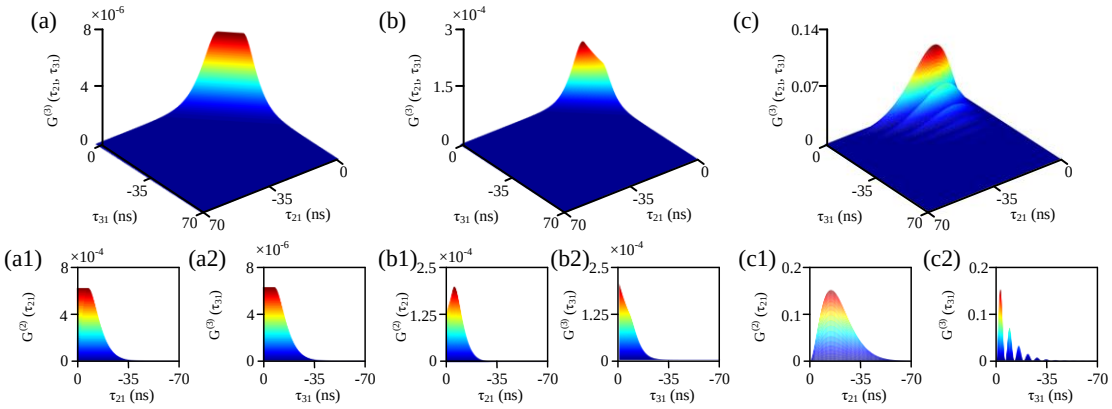

Figure S7. Simulation results of coincidence counts of time-energy-entangled W-triphoton state under various energy level coupling states. The upper panels (a–c) present the three-dimensional distribution of triphoton plotted in the (τ_{21}, τ_{31}) parameter space. The corresponding lower subfigures (a1–c1) and (a2–c2) display the conditional two-photon coincidence counts for (a-c) in τ_{21} and τ_{31} directions, respectively. (a) triphoton generated in the regime A in Figure 1(e) of the main part. (b) and (c) triphoton are generated in regimes AC and C, respectively. Simulation parameters are set as follows: $\Gamma_{54} = 2\pi \times 0.66$ MHz, $\Gamma_{31} = \Gamma_{41} = 2\pi \times 6$ MHz, $\Gamma_{11} = \Gamma_{22} = 0.4 \times \Gamma_{41}$, and $\Gamma_{21} = 0.2 \times \Gamma_{41}$.

As shown in Figure S7(c), the triphoton coincidence distribution corresponds to triphoton generation in the strongly coupled region labeled as state C in the phase diagram. In this regime, the $|4\rangle \leftrightarrow |5\rangle$ coupling supports coherent dynamics, giving rise to damped Rabi oscillations along the τ_{31} direction while maintaining antibunching along τ_{21}. This behavior is corroborated by the conditional two-photon coincidence counts in Figures S7(c1) and (c2), which clearly reveal oscillatory features associated with the strong-coupling non-Hermitian regime.

4. Time–Energy Entangled W-State Triphotons under various Coupling Regimes

In the SSWM process, triphotons are spontaneously generated in the SSWM process, denoted as ($\boldsymbol{E}_{S1}$), ($\boldsymbol{E}_{S2}$), and ($\boldsymbol{E}_{S3}$), which correspond to Alice, Bob, and Charlie in our experiment. The process is governed by strict energy conservation condition ($\omega_1 + \omega_2 + \omega_3 = \omega_{S1} + \omega_{S2} + \omega_{S3}$) and phase-matching condition ($k_1 + k_2 + k_3 = k_{S1} + k_{S2} + k_{S3}$). As a result, the individual photon energies (ω_{S1}), (ω_{S2}), and (ω_{S3}) are not independently determined; instead, they are intrinsically correlated. The triphoton state generated via SSWM is shown in Eq. (S26). The presence

of the global delta function is crucial: it enforces a fixed total energy while allowing each individual photon energy to fluctuate. This immediately implies genuine time–energy entanglement among all three photons.

A defining feature of W-class multipartite entanglement is that bipartite entanglement survives after conditioning on or tracing out one particle. In our system, when the energy of one photon—say, the photon (Alice)—is measured to be ω_{S1}, the remaining two photons (Bob) and (Charlie) are projected onto the conditional state

$$\left|\psi_{S_2S_3}^{\omega_{S1}}\right\rangle = \iint d\omega_{S2}d\omega_{S3}\chi^{(5)}\Phi(\tfrac{\Delta KL}{2})\delta(\Delta\omega)|\omega_{S2},\omega_1+\omega_2+\omega_3-\omega_{S1}-\omega_{S2}\rangle \tag{S35}$$

This state is non-separable in the energy–time degree of freedom, demonstrating that photons ($\boldsymbol{E}_{S2}$) and ($\boldsymbol{E}_{S3}$) remain entangled even after the energy of ($\boldsymbol{E}_{S1}$) is known. This persistence of bipartite entanglement under conditional measurement is a hallmark of W-class tripartite entanglement, in clear contrast to GHZ-type states, for which measuring one particle destroys all remaining entanglement.

Although the triphoton state is fundamentally generated as a continuous-variable time–energy entangled state, it can be equivalently expressed in a discrete, channel-based form that makes the W-class structure explicit.
Because the total energy (ω) is fixed, there exist three equivalent and indistinguishable conditional configurations:

- the energy of ($\boldsymbol{E}_{S1}$) is specified, leaving ($\boldsymbol{E}_{S2}$)–($\boldsymbol{E}_{S3}$) entangled,
- the energy of ($\boldsymbol{E}_{S2}$) is specified, leaving ($\boldsymbol{E}_{S1}$)–($\boldsymbol{E}_{S3}$) entangled,
- the energy of ($\boldsymbol{E}_{S3}$) is specified, leaving ($\boldsymbol{E}_{S1}$)–($\boldsymbol{E}_{S2}$) entangled.

These three configurations form a symmetric set of orthogonal conditional channel states ($|\psi_1\rangle$, $|\psi_2\rangle$, $|\psi_3\rangle$), and the total triphoton state can be written as their coherent superposition,

$$|\Psi_W\rangle = \tfrac{1}{\sqrt{3}}(|\psi_1\rangle + |\psi_2\rangle + |\psi_3\rangle) \tag{S36}$$

In the occupation-number representation of the three spatial modes (S1), (S2), and (S3), this is equivalent to the canonical W state $|\Psi_W\rangle = \frac{1}{\sqrt{3}}(|001\rangle + |010\rangle + |100\rangle)$. Where the three modes correspond exactly to the Alice–Bob–Charlie detection channels in the experiment. Thus, the W-class description is not an additional assumption but an equivalent representation of the same energy-conserving triphoton state in a different basis.

Figure S8 illustrates schematic representations of the generated triphoton state under various coupling conditions, each corresponding to a specific regime in the non-Hermitian phase space depicted in Figure 1(e) of the main text. These diagrams visualize the correlation relationship among three emitted photons (denoted E_{S1}, E_{S2} and E_{S3}), offering physical insight into how energy-level structure governs triphoton correlations.

Figure S8(a) shows the case where both E_{D1} and E_{D2} are absent, placing the system in the weak-coupling regime A. There is only one state for each photon in the W-state triphoton, and each photon correlation pathway involves one single coherent channel and two decay channels. The corresponding level diagram and triphoton correlation are presented in Figures 2(b) and 3(a), respectively. Figure S8(b) illustrates triphoton generation in a strong coupling state (regime B in Figure 1(e)) between $|2\rangle$ and $|4\rangle$, where energy-level $|4\rangle$ splits into two sub-levels, thus there are two sub-coherence channels for the generation of E_{S2}. This leads to enhanced quantum interference with two resonant channels. Thus, in the W state triphoton, there are two coherent channels for both $E_{S2} \leftrightarrow E_{S1}$ and $E_{S2} \leftrightarrow E_{S3}$ correlation. Figures 2(d) and 3(c) show the corresponding level structure and triphoton correlations.

Figure S8(c) represents the strong coupling state (regime C) between $|4\rangle$ and $|5\rangle$. Here, the level $|5\rangle$ splitting leads to two excitation branches for photon E_{S3}, supporting two resonant channels in the generation of E_{S3}. In the correlation of triphoton, both $E_{S3} \leftrightarrow E_{S1}$ and $E_{S2} \leftrightarrow E_{S3}$ contain two coherent channels. This configuration gives rise to damped Rabi oscillations, as shown in Figure 3(e), and energy level structure in Figure 2(f). Figure S8(d) illustrates the generated triphoton state where both Rabi frequency of E_{D1} and E_{D2} are strong, corresponding to regime D. Both generation of E_{S2} and E_{S3} photons exhibit dual-resonance channels enabled by strong coupling-induced level splitting. E_{S2} and E_{S3} engage in two resonance channels and one absorptive channel. In the generated triphoton state, both $E_{S3} \leftrightarrow E_{S1}$ and $E_{S2} \leftrightarrow E_{S1}$ contain two coherent channels, $E_{S3} \leftrightarrow E_{S2}$ contains four coherent channels.

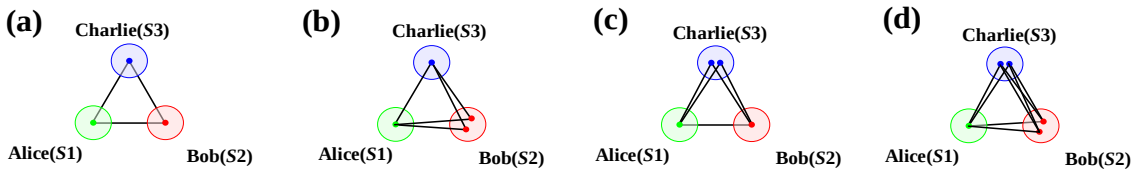

Figure S8. Time-energy-entangled W-triphoton state under the various energy level coupling states.

5. Additional detection of diagnose photons E_D

To further validate that the detected photons originate from SSWM, we conducted an additional detection of the two-photon coincidences E_{S3} and E_D simultaneously in conjunction with the coincidences between E_{S1} and E_{S2} by artificially introducing the diagnosed photons E_D. In our experiment, the detection direction of E_D is deliberately chosen to lie outside the phase-matching condition of the SSWM process. As a result, the signal observed in this channel primarily arises from background sources such as stray photons in the laboratory environment, photons generated via Raman scattering in the Rb vapor cell, and dark counts from the single-photon counting module. Crucially, E_D photons have no intrinsic quantum correlation with the genuine triphoton events produced via the SSWM process, and thus serve as an effective diagnostic probe to identify and suppress spurious threefold coincidences. To illustrate the functioning of each two-photon coincidence counting component, Figures S9a-c showcases a representative set of experimental data collected over a span of 20 minutes, employing a time bin width of 0.25 ns for each SPCM.

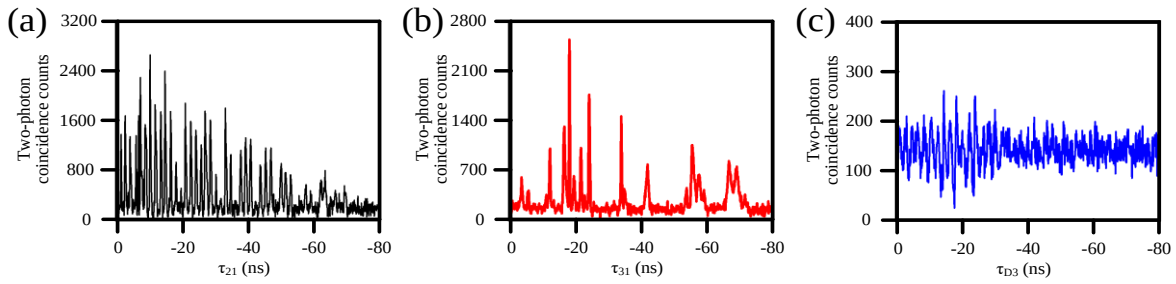

Figure S9. (**a**-**c**) the recorded two-photon coincidence counts, respectively, by SPCM1 and SPCM2, SPCM1 and SPCM3, and SPCM3 and SPCMD. These trigger events are plotted against the relative time differences (τ_{21}, τ_{31} and τ_{D3}) between clicks of the two respetive single-photon detectors.

References

[1] Li SF, Li YF, Xiong SQ, et al. Coherent Control of Multiphoton Using Multidressing Fields[J]. Annalen der Physik, 2021, 533(12):2100083.

[2] Li KK, Wen JM, Cai Y, et al. Direct generation of time-energy-entangled W triphotons in atomic vapor[J]. Science Advances, 2024, 10(37):eado3199.

[3] Yan H, Zhang S, Chen JF, et al. Generation of Narrow-Band Hyperentangled Nondegenerate Paired Photons[J]. Physical Review Letters, 2011, 106(3):033601.

[4] Li YM, Li KK, Ning SH, et al. Shaping the Temporal Waveform of Tri-Photon with Double-Dressing[J]. Annalen der Physik, 2021, 533(4):2000489.

[5] Zhao LW, Su YM, Du SW. Narrowband biphoton generation in the group delay regime[J]. Physical Review A, 2016, 93(3):033815.

[6] Jiang Y, Mei Y, Zuo Y, et al. Anti-Parity-Time Symmetric Optical Four-Wave Mixing in Cold Atoms[J]. Physical Review Letters, 2019, 123(19).
[7] Cao W, Lu X, Meng X, et al. Reservoir-Mediated Quantum Correlations in Non-Hermitian Optical System[J]. Physical Review Letters, 2020, 124(3).
[8] Li KK, Cai Y, Wu J, et al. Three-Body Topology Entanglement Generation via a Six-Wave Mixing: Competing and Coexisting of Linear and Nonlinear Optics Responses in Triphoton Temporal Correlation[J]. Advanced Quantum Technologies, 2020, 3(5):1900119.
[9] Wen JM, Xu P, Rubin MH, et al. Transverse correlations in triphoton entanglement: Geometrical and physical optics[J]. Physical Review A, 2007, 76(2):023828.
[10] Zhang SQ, Tang HT, Wei JJ, et al. One-Step Generation of Energy-Time-Polarization-Hyper-Entangled W-Class Triphotons: Nonlinear and Linear Optical Responses[J]. Annalen der Physik, 2023, 535(11):2300208.
[11] Li KK, Li SF, Li CB, et al. Dressing-Shaped Rabi Oscillation of Photon Pairs in Hot Atomic Ensemble[J]. Advanced Quantum Technologies, 2020, 4(2):2000098.
[12] Ahmed I, Zhang Z, Wen F, et al. Switching Correlation and Noise Level in Pr3+:YSO Crystal via Dressing Nonlinear Phase[J]. Scientific Reports, 2016, 6(1):33568.
[13] Zhang YP, Wang ZG, Nie ZQ, et al. Four-Wave Mixing Dipole Soliton in Laser-Induced Atomic Gratings[J]. Physical Review Letters, 2011, 106(9):093904
[14] Shu C, Chen P, Chow TKA, et al. Subnatural-linewidth biphotons from a Doppler-broadened hot atomic vapour cell[J]. Nature Communications, 2016, 7(1):12783
[15] Du SW, Wen JM, Rubin MH. Narrowband biphoton generation near atomic resonance[J]. Journal of the Optical Society of America B: Optical Physics, 2008, 25(12):C98-C108.